Modeling the OEC with Two New Biomimetic Models: Preparations, Structural Characterization, and Water Photolysis Studies of a Ba–Mn Box Type Complex and a Mn₄N₆ Planar-Diamond Cluster

Lara Rouco [1], **M. Isabel Fernández-García [1]**, **Rosa Pedrido [2]**, **Luis M. Botana [3]**, **David Esteban-Gómez [4]**, **Carlos Platas-Iglesias [4]** and **Marcelino Maneiro [1,*]**

[1] Departamento de Química Inorgánica, Facultade de Ciencias, Universidade de Santiago de Compostela, 27002 Lugo, Spain; lara.rouco.mendez@usc.es (L.R.); misabel.fernandez.garcia@usc.es (M.I.F.-G.)

[2] Departamento de Química Inorgánica, Facultade de Química, Universidade de Santiago de Compostela, 15782 Santiago de Compostela, Spain; rosa.pedrido@usc.es

[3] Departament of Pharmacology, Faculty of Veterinary, University of Santiago de Compostela, 27002 Lugo, Spain; luis.botana@usc.es

[4] Centro de Investigacións Científicas Avanzadas (CICA) and Departamento de Química, Campus Zapateira, Universidade da Coruña, 15008 A Coruña, Spain; david.esteban@udc.es (D.E.-G.); carlos.platas.iglesias@udc.es (C.P.-I.)

* Correspondence: marcelino.maneiro@usc.es; Tel.: +34-982-824-106

check for updates

Abstract: The oxygen-evolving complex (OEC) is the native enzyme that catalyzes the oxidation of water in natural photosynthesis. Two new classes of manganese cluster complexes of formula $Ba_2Mn_2L^1_2(H_3L^1)_2(CH_3OH)_4$ **1** and $Mn_4L^2_6Cl_2$ **2** were prepared ($H_4L^1 = N,N'$-(ethane-1,2-diyl)bis (2-hydroxybenzamide); L^2 = methyl picolinimidate) and characterized by standard techniques including microanalysis, IR spectroscopy, ESI spectrometry, and magnetic susceptibility measurements. X-ray diffraction studies of these complexes revealed (i) a box-type structure for **1** formed by two redox-active manganese(III) ions and two barium(II) ions connected by two bridging *bis*amido-bisphenoxy ligand molecules; and (ii) a planar-diamond array for Mn_4N_6 cluster **2** where the picolinimidates act as chelating ligands through the two nitrogen atoms. The ability of **1** and **2** to split water has been studied by means of water photolysis experiments. In these experiments, the oxygen evolution was measured in aqueous media in the presence of *p*-benzoquinone (acting as the hydrogen acceptor), the reduction of which was followed by UV-spectroscopy. The relevant photolytic activity found for **1** is in contrast to the inactivity of **2** in the photolytic experiments. This different behavior is discussed on the basis of the structure of the biomimetic models and the proposed reaction mechanism for this process supported by DFT calculations.

Keywords: artificial photosynthesis; photocatalyst; water splitting; manganese

1. Introduction

The oxygen-evolving complex (OEC) is the catalytic site that catalyzes, in natural photosynthesis, the oxidation of water into dioxygen, protons, and electrons [1–3]. The native Mn_4CaO_5 complex, located at the donor site of photosystem II (PSII), is responsible for both the atmospheric oxygen that we breathe, and also the conversion of solar energy into chemical energy. In this process, water splitting is the key step that drives the chain of electron-transduction reactions to form the energy transporting molecule NADPH, which holds the electrons in this chain [4,5]. The natural catalyst contains four

manganese atoms and one calcium atom, coordinated by four water molecules, one imidazole, and six carboxylate groups. In addition, two chloride ions are also in the vicinity of the Mn_4Ca cluster [1,6]. Much of what we know about this catalytic complex was learned through structural and functional artificial models of the OEC [7–10]. Structural understanding of this catalytic site has been achieved thanks to multiple techniques, such as EPR [11–13], XAS [14–16] or XRD [17,18], often based on the information obtained through mimetic models. The understanding of the mechanism of water oxidation is also better understood on the basis of data obtained from bioinorganic modeling of the OEC [19–21].

We have previously reported that a number of manganese model compounds are catalysts for water photolysis [22,23]. In this sense, manganese-Schiff base μ-aqua dimers were found to be active systems under light irradiation and in the presence of p-benzoquinone, which acts as a hydrogen acceptor. The ONNO set of the tetradentate-Schiff base (using the iminic nitrogen and phenoxy oxygen atoms) provides a strong chelating effect which confers an increased robustness to this type of complex in comparison to other systems [24,25]. We propose a mechanism for this catalysis involving successive hydrogen abstractions from water molecules bound to the metal ions by optically excited p-benzoquinone. Photogenerated dioxygen is evolved in the overall process, while p-benzoquinone is reduced to hydroquinone (Scheme 1).
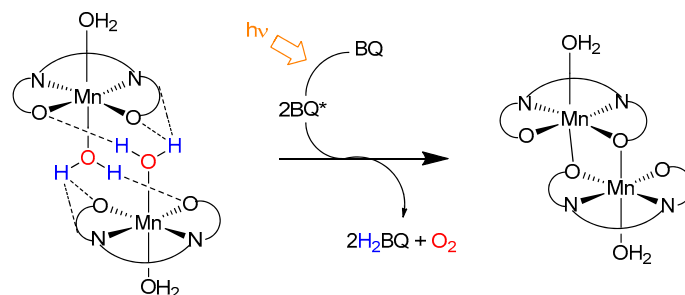
Scheme 1. Photogeneration of dioxygen from water molecules bound to the metal ion in manganese-Schiff base μ-aqua dimers.

In our search for more efficient catalysts, we are looking for systems with higher nuclearity, different topologies, and other donor atoms beyond the iminic nitrogen or the phenoxy oxygen atoms. We are also interested in checking the hypothesis of the ease of coordination of the water molecules to achieve active catalysts. In order to address some of these issues, in the work described here, we report on two new potential biomimetic models of the OEC using other type of organic ligands, such as the *bis*amido-bisphenoxy H_4L^1 or the methyl-picolinimidate L^2 (see Scheme 2). H_4L^1 contains six potential donor atoms: two amide nitrogen, two phenoxy, and two amide oxygen atoms. The latter donor atoms point outward with respect to the ligand cavity which may facilitate the extension of the structure dimensionality. In addition, the synthetic procedure used to obtain the manganese complex incorporates an alkaline earth metal (i.e., barium) which may be important in stabilizing the structure taking into account the presence of other alkaline earth metal ion, calcium, in the natural OEC. In the case of the L^2 ligand, its structure may favor the formation of high-nuclearity clusters.
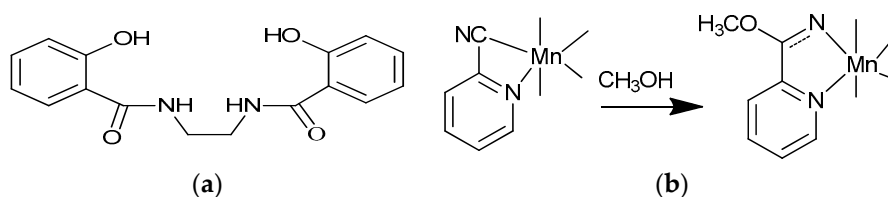
Scheme 2. (**a**) Structure of H_4L^1. (**b**) Methanolysis process to explain the formation of the L^2 ligand from the initial 2-cyanopyridine.

2. Results

2.1. Preparation and Characterization of Biomimetic Model 1

The multidentate *bis*amido-*bis*phenoxy H_4L^1 readily reacts with manganese(II) acetate in the presence of barium hydroxide and air, as detailed in the experimental section, to give biomimetic model **1** $(Ba_2Mn_2L^1{}_2(H_3L^1)_2(CH_3OH)_4)$. The alkaline earth-metal hydroxide provides the basic conditions required to achieve tetradeprotonation of the ligand and oxidation of manganese(II) to manganese(III) in the presence of oxygen. Elemental analysis of the complex indicated a stoichiometry $Ba_2Mn_2L^1{}_2(H_3L^1)_2(CH_3OH)_4$, which is consistent with the formation of neutral species, where L identifies the ligand in its tetra-anionic form, and H_3L identifies the ligand in its monoanionic form. The analytical, magnetic, spectroscopic, and mass spectrometry data for model **1** are given in the Materials and Methods section. Complex **1** seems to be stable in air as well as thermally stable, melting above 300 °C without decomposition. It is sparingly soluble in water, partially soluble in common organic solvents such as methanol, and very soluble in polar coordinating solvents such as DMF and DMSO. The formulation of model **1** is in agreement with the molar conductivity measured in 10^{-3} M DMF solution, which is 23 μS cm^{-1}, typical of non-electrolyte complexes [26].

The value for the magnetic moment at room temperature, 4.8 B.M., is very close to the spin-only value of 4.89 B.M. expected for a high-spin magnetically diluted d^4 manganese(III) ion. The ESI (electrospray ionization) mass spectrum (Figure 1) registered in methanol shows a peak corresponding to the fragment $[MnL + H^+]^+$, indicating coordination of the manganese ion with the deprotonated ligand. Other minor signals, assigned to $[MnL(H_3L) + H^+]^+$, $[Mn_2L(H_3L) + H^+]^+$, $[MnL(H_3L)Ba + H^+]^+$ and $[MnL(H_3L)Ba_2 + H^+]^+$ also confirm the formation of the polynuclear complex including manganese, barium, and the ligand both in its tetra-anionic (L^{-4}) and monoanionic (H_3L^-) forms. IR spectroscopy also suggests the formation of model **1**, exhibiting the set of bands attributable to the tetra-anionic coordinated ligand, but also the corresponding bands that can be assigned to the monoanionic form of the ligand. Thus, the strong band at 1605 cm^{-1}, characteristic of the ν(amide)I (C=O) stretching mode, is shifted 38 cm^{-1} to lower wavenumbers with respect to the free ligand (1643 cm^{-1}), and the band 1540 of the ν(amide)II stretching mode, is shifted 12 cm^{-1} with respect to the free ligand (1552 cm^{-1}). These data suggest coordination of the L^{-4} ligand through the amide nitrogen atoms, but additional bands at 1641 cm^{-1} and 1551 cm^{-1} can be assigned to the H_3L^- ligand which does not coordinate through these amide nitrogen atoms. The band attributed to the ν(C–O) mode is also shifted 11 cm^{-1} to lower frequencies with respect to the free ligand, indicating coordination through the hydroxyl groups. A strong band centered at ca 3400 cm^{-1} can be assigned to the ν(O–H) of methanol molecules.
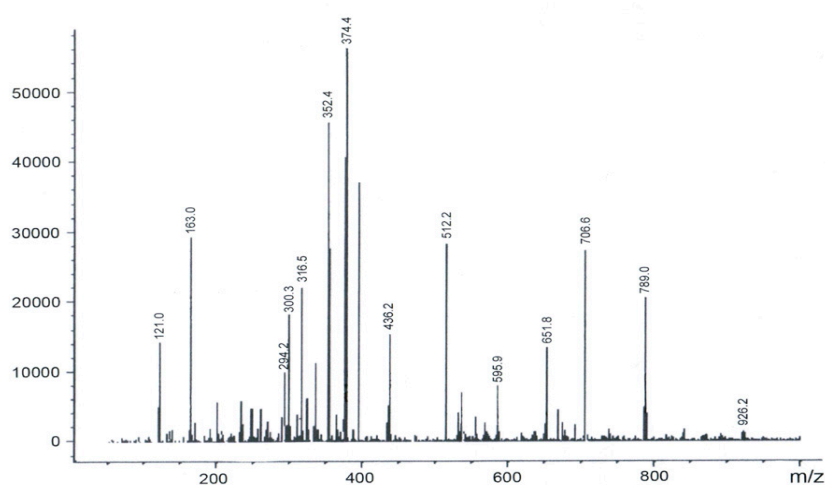

Figure 1. Electrospray ionization (ESI) mass spectrum for complex **1**.

The electronic absorption spectrum of **1** shows two broad bands: a broad shoulder obtained at 510 nm (ε = 700 M^{-1} cm^{-1}), attributable to a d–d transition, and a broad band at 484 nm (ε = 3100 M^{-1} cm^{-1}), assigned to the phenolate $\rightarrow$ manganese(III) charge transfer. The energy and intensity of these two bands are in agreement with those reported for related manganese(III) complexes [27,28]. The paramagnetic ^1H NMR spectrum (Figure S1 contains an up-field proton resonance outside the diamagnetic region at –24.17 ppm (Figure S1) due to the isotropic shifting of the ligand protons for high-spin manganese(III) complexes in an octahedral field. This signal corresponds to the protons in ortho positions relative to the hydroxyl groups [22,23,29] and serves to substantiate the formation of a manganese(III) complex.

Single crystals of complex **1** suitable for X-ray diffraction studies were obtained as described in the Materials and Methods section. The main crystal data and structure refinement details are shown in Tables 1 and 2; detailed crystallographic data is shown in Tables S1–S5 of the Supplementary Materials. Different drawings showing the crystal structure are shown in Figures 2 and 3.

Table 1. Crystal data and structure refinement parameters for compounds **1** and **2**.

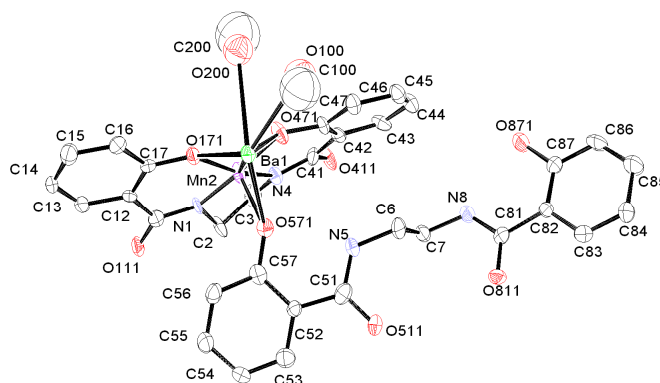| Compound	1	2
Empirical formula	$C_{34}H_{35}BaMnN_4O_{10}$	$C_{21}H_{24}ClMn_2N_6O_3$
Formula weight	851.93	553.79
Temperature (K)	100(2)	293(2)
Wavelength (Å)	0.71073	0.71069
Crystal system	Monoclinic	Monoclinic
Space group	$P2_1/c$	$P2_1/n$
a (Å)	12.245(2)	11.953(5)
b (Å)	17.345(3)	11.256(5)
c (Å)	18.041(4)	17.889(5)
α (°)	90	90
β (°)	106.38(3)	99.051(5)
γ (°)	90	90
Volume ($Å^3$)	3676.2(13)	2376.9(16)
Z	4	4
$D_{calcd.}$ (g cm^{-3})	1.525	1.548
μ (mm^{-1})	1.467	1.21
F (000)	1712	1132
$\theta_{min/max}$ (°)	2.62/21.14	1.92/24.73
Goodness-of-fit on F^2	1.005	1.067
Total data	27,410	4038
Unique data	6303	4038
Data/restrains/parameters	6303/3/440	4038/0/299
Final R indices ($I > 2\sigma(I)$)	R_1 = 0.0521; wR_2 = 0.1220	R_1 = 0.0894; wR_2 = 0.2658
R indices (all data)	R_1 = 0.0941; wR_2 =0.1356	R_1 = 0.1223; wR_2 =0.2812

Figure 2. ORTEP view for the $BaMnL^1(H_3L^1)(CH_3OH)_2$ asymmetric unit for compound **1**, with atoms showing the atomic numbering scheme.

Table 2. Selected bond lengths (Å) and angles (°) for **1**.

|			
Mn(2)–N(1)	1.938(5)	Ba(1)–O(411)	2.636(5)
Mn(2)–N(4)	1.944(6)	Ba(1)–O(511)	2.648(5)
Mn(2)–O(471)	1.877(5)	Ba(1)–O(811)	2.658(5)
Mn(2)–O(171)	1.883(5)	Ba(1)–O(171)	2.754(5)
Mn(2)–O(571)	2.125(5)	Ba(1)–O(471)	2.816(5)
Ba(1)–Mn(2)	3.5510(12)	Ba(1)–O(571)	3.074(5)
		Ba(1)–O(200)	
		Ba(1)–O(100)	
O(471)–Mn(2)–O(171)	88.6(2)	O(411)–Ba(1)–O(511)	120.81(16)
O(471)–Mn(2)–N(1)	173.4(2)	O(411)–Ba(1)–O(811)	75.91(14)
O(171)—Mn(2)–N(1)	92.4(2)	O(511)–Ba(1)–O(811)	91.95(14)
O(471)—Mn(2)–N(4)	92.7(2)	O(411)–Ba(1)–O(171)	97.69(15)
O(171)—Mn(2)–N(4)	164.2(2)	O(511)–Ba(1)–O(171)	140.07(14)
N(1)–Mn(2)–N(4)	84.6(2)	O(811)–Ba(1)–O(171)	87.29(14)
O(471)–Mn(2)–O(571)	84.4(2)	O(411)–Ba(1)–O(471)	139.51(16)
O(171)–Mn(2)–O(571)	92.40(19)	O(511)–Ba(1)–O(471)	94.13(15)
N(1)–Mn(2)–O(571)	102.1(2)	O(811)–Ba(1)–O(471)	126.37(14)
N(4)–Mn(2)–O(571)	103.4(2)	O(171)–Ba(1)–O(471)	56.24(14)
		O(411)–Ba(1)–O(571)	142.68(14)
		O(511)–Ba(1)–O(571)	82.08(13)
		O(811)–Ba(1)–O(571)	74.13(13)
		O(171)–Ba(1)–O(571)	59.34(13)
		O(471)–Ba(1)–O(571)	54.23(13)
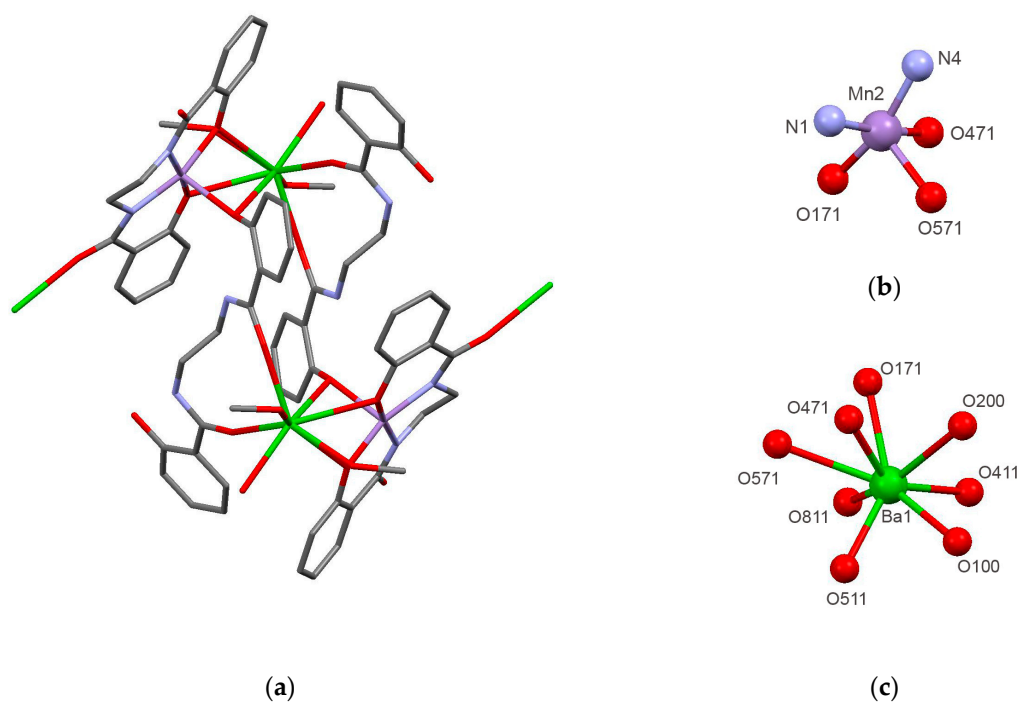
Figure 3. (**a**) Stick diagram of supramolecular box **1** (barium cation in green, manganese ion in purple, oxygen in red, nitrogen in blue, and carbon in grey); (**b**) coordination environment around the manganese center in **1**, showing the square-pyramidal geometry for this ion; (**c**) coordination environment around the barium center in **1**.

The asymmetric unit comprises a barium ion, a manganese ion, a tetraanionic $(L^1)^{4-}$ ligand, a monoanionic $(H_3L^1)^-$ entity, and a methanol solvent molecule. The two manganese ions of **1** have similar coordination environments.

The geometry around the manganese(III) ion is a five-coordinated distorted square-pyramidal geometry (Figure 3b). The coordination sphere around each manganese center comprises the planar tetraanionic *bis*amido-bisphenoxy L^{4-} ligand, which is tightly bound to the metal ion through the inner N_2O_2 compartment by the N_{amide} and O_{phenol} atoms. The Mn-N_{amide} (1.938 Å and 1.944 Å) and Mn-O_{phenol} (1.877 Å and 1.883 Å) bond lengths are in the range expected for the tetradeprotonation of the ligand [23]. The fifth coordination position is completed with a phenolic oxygen atom (O571) from a monoanionic (H_3L^1) ligand. Thus, two different coordination behaviors are found in **1** for the parent *bis*amido-bisphenoxy ligand: the inner compartment of the tetra-anionic $(L^1)^{4-}$ forms three chelate rings (two six-membered and one five-membered) once the manganese ion is coordinated, while the monoanionic $(H_3L^1)^-$ ligand coordinates to one position of the manganese ion coordination environment, acting as a bridging ligand between the manganese ion and the farthest barium ion. The axial Mn–O571 length of 2.125 Å is longer than the other Mn–O_{phenol} lengths due to the Jahn–Teller effect derived from the Mn(III) d^4 high-spin configuration. The angles between the O–(or N)–Mn–O571, representing O or N donor atoms at the equatorial positions occupied by the inner N_2O_2 compartment of $(L^1)^{4-}$, range from 84.4° to 103.4°, revealing certain distortions of the square-pyramidal geometry around each Mn(III) ion. Moreover, the amide atoms of $(H_3L^1)^-$ and $(L^1)^{4-}$, which point towards the outside of the inner cavity, play crucial roles in to extending the dimensionality of the structure, since they are bound to the barium ions.

The two barium atoms of **1** have similar coordination environments. The barium atom is bound to eight oxygen atoms (Figure 3c): two phenoxy oxygen atoms (O171 and O471) from the tetra-anionic L^{4-} ligand, also bound to the manganese ion; two methanolic oxygen atoms (O100 and O200); and three amidic oxygen atoms (O411, O511, and O811) from two different neighboring ligands, $(L^1)^{4-}$ and $(H_3L^1)^-$. Therefore, each barium atom is coordinated with four different residues, which results in Ba–O distances ranging from 2.636 to 3.073 Å. The relatively broad range of Ba–O distances is also associated with increased structural flexibility and an increased capacity for close contacts between the barium ion and aromatic rings [30]. Nevertheless, these distances are also in the expected range for Ba–O bonds [31].

The barium atoms and the bridging $(H_3L^1)^-$ ligands play crucial roles in the assembly of the final supramolecular structure of **1**, which can be also visualized as a $Ba_2Mn_2L^1{}_2(H_3L^1)_2(CH_3OH)_4$ supramolecular box (Figure 3a). The size of the cavity inside the box is larger than those displayed by supramolecular boxes induced by alkali metal ions [23]. Thus, the Ba–Ba distance in **1** is 8.339 Å, while the M–M distances for alkali metal ions range from 4.47 to 4.87 Å for potassium, rubidium, and cesium supramolecular boxes. The distance between the manganese ions is 7.886 Å, which is long enough to prevent intermetallic interactions to be established, in agreement with the observed spin-only magnetic moment of 4.8 B.M.

2.2. Preparation and Characterization of Biomimetic Model 2

The reaction of 2-cyanopyridine and Mn(II) in methanol solution leads to the formation of biomimetic model **2** ($Mn_4L^2{}_6Cl_2$) containing *O*-methyl picolinimidate L^2 as the chelate ligand. The methanolysis of the initial 2-cyanopyridine takes place upon coordination with the Mn(II) ion as a chelating bidentate ligand through the two nitrogen atoms of the pyridine ring and the carbonitrile group. As observed previously, the coordination of 2-cyanopyridine to some divalent metal ions activates the CN triple bond and makes it much more amenable toward nucleophilic attack by CH_3OH molecules [32–34]. The proposed stoichiometry for complex **2**, $Mn_4L^2{}_6Cl_2$, in which six *O*-methyl picolinimidate ligands are in a monoanionic mode $(L^2)^-$, was confirmed by analytical and spectroscopic data. Moreover, recrystallization from the mother liquors afforded X-ray quality crystals for **2**. Complex **2** melts above 300 °C without decomposition. It is insoluble in water and sparingly soluble in common organic solvents such as methanol, but soluble in polar coordinating solvents such as DMF and DMSO. The molar conductivity measurement in 10^{-3} M DMF solution of 18 µS cm^{-1} is also consistent with the formation of the neutral $Mn_4L^2{}_6Cl_2$ species [26]. The value of the room

temperature magnetic moment with diamagnetism corrections is 5.6 B.M., which is compatible with high-spin magnetically diluted d^5 manganese(II) ions. This value does not allow for differentiation between octahedral and bipyramid trigonal coordination modes, since the ligand field theory raises the same number of unpaired electrons in both types of geometries.

The ESI-MS of the CH_2Cl_2 solution of **2** gives peaks at *m/z* 1108.4 and 1129.5, which corresponds to [**2** + H]$^+$ and [**2** + Na]$^+$ (positive mode), suggesting the stability of this biomimetic model in solution (Figure S2). The IR spectrum for **2** also confirms the methanolysis reaction of the 2-cyanopyridine to give the *O*-methyl picolinimidate ligand. Thus, the spectrum (Figure S3) has a sharp band with a medium intensity at 3237 cm^{-1}, characteristic of the N–H vibration of *O*-methyl picolinimidate [35]. The C–H stretching vibrations of the methyl groups of the carboxamide appear at 2981 and 2940 cm^{-1}, while the absence of the $\nu(C\equiv N)$ band (which should have appeared at about 2240 cm^{-1}) is indicative that the nitrile group has been converted to a carboxamide one. An additional strong band at 1659 cm^{-1} is also assigned to $\nu(C=NH)$ of the carboxamide group. The C–H stretching vibrations of the pyridine rings appear at 3072 cm^{-1}. Different medium and strong bands observed in the range 1631–1591 cm^{-1} are assigned to C=N, C=C, and C–C stretching vibrations [36]. The absorption band at 1379 cm^{-1} is assigned to the $\nu(=C–O–)$ stretching vibration which mixes with $\delta(NH)$ of the imino ether group. The $\nu_{as}(C–O–C)$ and $\nu_s(C–O–C)$ absorption bands appear at 1138 and 965 cm^{-1}, respectively. The absorption band observed at 1206 cm^{-1} is assigned to $\delta(O–CH_3)$. The medium absorption band observed at the far-infrared spectrum region at 303 cm^{-1} is assigned to Mn–Cl stretching vibrations [37], indicating the coordination of the chloride to the manganese ions.

Single crystals of complex **2**, suitable for X-ray diffraction studies, were obtained by slow evaporation of the mother liquors at room temperature. The main crystal data and structure refinement details are collected in Tables 1 and 3; detailed crystallographic data is collected in Tables S6–S10. Figures 4 and 5 show different views of the structure of **2**, which displays a planar-diamond core of the tetrameric cluster. The creation of bioinspired catalysts to reproduce the basic chemistry of the natural OEC has aroused great interest in the preparation of tetranuclear manganese clusters [3,7,9,10,13,15,38–43].

Table 3. Selected bond lengths (Å) and angles (°) for **2**.

Mn(1)–N(28)	2.048(8)	Mn(1)–Mn(2)#1	3.206(2)
Mn(1)–N(8)	2.051(8)	Mn(2)–N(28)#1	1.939(8)
Mn(1)–N(18)#1	2.120(7)	Mn(2)–N(8)	1.971(8)
Mn(1)–N(1)	2.123(9)	Mn(2)–N(11)	2.081(11)
Mn(1)–N(18)	2.141(8)	Mn(2)–Cl(31)	2.305(4)
Mn(1)–N(21)	2.143(10)	Mn(2)–N(18)	2.353(8)
Mn(1)–Mn(2)	3.203(2)	Mn(2)–Mn(1)#1	3.206(2)
N(28)–Mn(1)–N(8)	175.2(3)	N(28)#1–Mn(2)–N(8)	124.9(4)
N(28)–Mn(1)–N(18)#1	80.3(3)	N(28)#1–Mn(2)–N(11)	118.5(4)
N(8)–Mn(1)–N(18)#1	102.2(3)	N(8)–Mn(2)–N(11)	101.3(4)
N(28)–Mn(1)–N(1)	98.5(3)	N(28)#1–Mn(2)–Cl(31)	101.6(2)
N(8)–Mn(1)–N(1)	77.1(3)	N(8)–Mn(2)–Cl(31)	102.9(2)
N(18)#1–Mn(1)–N(1)	98.9(3)	N(11)–Mn(2)–Cl(31)	105.2(3)
N(28)–Mn(1)–N(18)	102.7(3)	N(28)#1–Mn(2)–N(18)	76.8(3)
N(8)–Mn(1)–N(18)	81.9(3)	N(8)–Mn(2)–N(18)	78.4(3)
N(18)#1–Mn(1)–N(18)	78.2(3)	N(11)–Mn(2)–N(18)	75.4(4)
N(1)–Mn(1)–N(18)	157.7(3)	Cl(31)–Mn(2)–N(18)	178.4(2)
N(28)–Mn(1)–N(21)	77.9(4)		
N(8)–Mn(1)–N(21)	100.4(4)		
N(18)#1–Mn(1)–N(21)	155.7(4)		
N(1)–Mn(1)–N(21)	94.8(4)		
N(18)–Mn(1)–N(21)	96.2(4)		
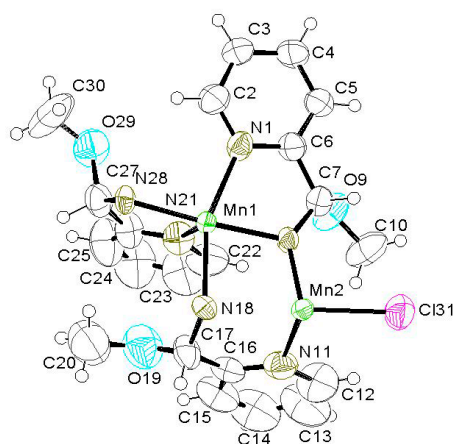
Figure 4. ORTEP view for the asymmetric unit for **2** with atoms showing the atomic numbering scheme.
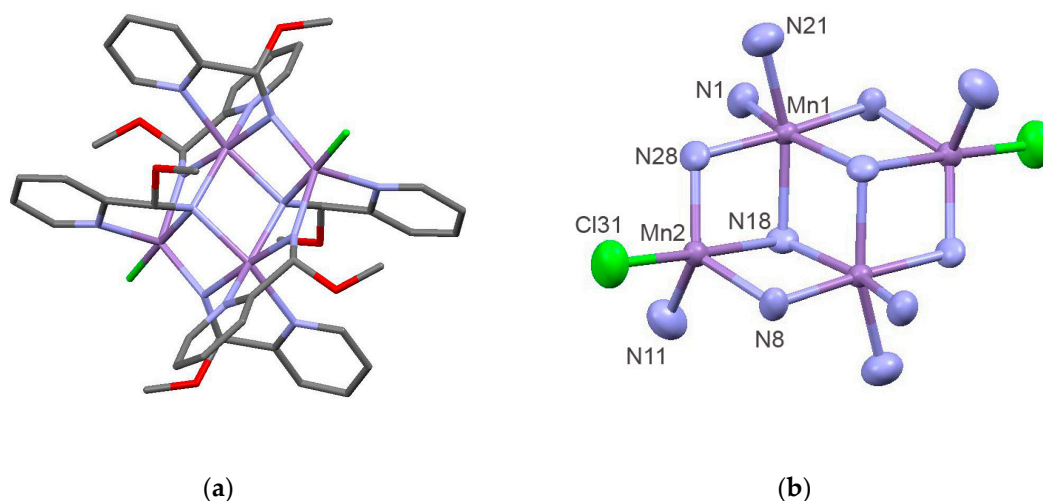

|(**a**)|(**b**)|

Figure 5. (**a**) Stick diagram of planar-diamond cluster 2. (**b**) Planar-diamond cluster core showing the atomic numbering scheme.

The biomimetic model $Mn_4L^2_6Cl_2$ (**2**) contains six *O*-methyl picolinimidate and two chloride ligands. The structure of **2** also reveals the decomposition of the 2-cyanopyridine via the addition of methanol across the C≡N triple bond to form a chelating ligand *O*-methyl picolinimidate $(L^2)^-$.

The coordination numbers are six and five for Mn1 and Mn2, respectively. The metal coordination geometry is described as distorted octahedral for Mn1 and distorted trigonal bipyramidal for Mn2 [44]. Analysis of the shape determining angles for Mn2, using the approach of Reedijk and coworkers [45], yielded τ [$(\alpha$-$\beta)/60$, being with α and β being the two greatest valence angles of the coordination center] having a value of 0.9 for Mn2 ($\tau = 0.0$ and 1.0 for square-pyramidal and trigonal bipyramidal geometries respectively). Thus, if we apply the same approach for the five-coordinated manganese ion in **1**, we obtain a value of 0.15 for τ, corresponding to the described square-pyramidal geometry. Although M(II) metal complexes tend to stabilize in octahedral geometries, which is the case for Mn1 in **2**, the symmetrical high-spin configuration of the Mn(II) ion provides no crystal field stabilization energy (CFSE), and the stability constants of its high-spin complexes are consequently lower than those of corresponding complexes of neighboring M(II) ions. This may be one of the reasons for the occurrence of different geometries such as the trigonal bipyramidal displayed by Mn2 in **2**.

Each manganese atom in **2** is coordinated to three or four different *O*-methyl picolinimidate ligands, depending on whether the ion is trigonal bipyramidal or octahedral. In the case of Mn1, which has a octahedral geometry, two chelating $(L^2)^-$ are bound via the pyridyl nitrogen donor (Mn1–N1 = 2.123(9) Å and Mn1–N21 = 2.143(10)) and the imine nitrogen atoms (Mn1–N8 = 2.051(8) Å

and Mn1–N28 = 2.048 Å), two additional monodentate $(L^2)^-$ ligands are also bound through their imine nitrogen atoms (Mn1–N18 = 2.141(8) and 2.120(7) Å). For Mn2, three $(L^2)^-$ are bound; one of them behaves as the chelating ligand through the pyridyl and the imine nitrogen atoms (Mn2–N11 = 2.081(11) Å and Mn2–N18 = 2.353(8) Å), while two $(L^2)^-$ act as monodentates via the imine nitrogen atoms (Mn2–N28 = 1.939(8) and Mn2–N8 = 1.971(8)). The fifth coordination position for Mn2 is completed with a chloride ion. Accordingly, each one of the six *O*-methyl picolinimidate ligands chelates a manganese ion but also bridges two manganese centers via the imine nitrogen atom.

2.3. Photolytic Studies

The photolytic experiments were carried out in the presence of p-benzoquinone, a water-soluble hydrogen atom acceptor [46]. The experimental details are given in Section 4.5, and the experimental setup was improved by us [22,23] with respect to previous experiments [47,48] in order to obtain a better sealing of the system. The magnetic stirrer used in the original experimental setup had a detrimental effect on the reproducibility of the dissolved oxygen measurements, while now the use of a methacrylate bath allows magnetic stirring, so the setup is more airtight.

The photolytic activity of the biomimetic models was followed in two ways: quantitative oxygen evolution and variation of the electronic spectrum of the BQ during photolysis. It was noted earlier that excited-state benzoquinone abstracts a hydrogen atom directly from water [49] at pH 7 and is greater in aqueous solutions. The final products were hydroquinone and 2-hydroxybenzoquinone.

The concentrations of O_2 in the solutions during the experiments increased linearly from about 2% dissolved oxygen to 14.4% for photolysis catalyzed by biomimetic model **1**, whereas the concentrations of O_2 remained almost constant for hours in the case of photolytic experiments using biomimetic model **2** (Figure 6). The ability of **1** to split water was also been tested by the reduction of p-benzoquinone into hydroquinone, which was determined by spectrophotometric monitoring of the reaction. Benzoquinone in water has major absorption at 246 nm ($\varepsilon = 2.2 \times 10^4$ M^{-1} cm^{-1}), which decreased during the experiments, whilst a characteristic hydroquinone peak at 290 nm developed (Figure 7).
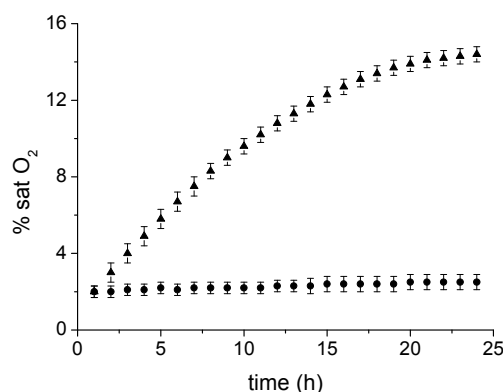

Figure 6. Plot of the percentage of O_2 dissolved in solution vs time for complexes 1 (▲) and 2 (●).

The photolytic experiment for **2** showed similar behavior to an aqueous solution containing only benzoquinone (without any complex)—a slow decrease in the amount of benzoquinone, followed by the formation of a mixture of hydroquinone and 2-hydroxy-p-benzoquinone without the generation of molecular oxygen [49]. The fact that 2-hydroxy-p-benzoquinone was not observed in the UV-VIS spectrum for the present studies with **1** indicates that it is probably stabilized by the manganese complex, presumably due to the approaching of the quinones to the complex. In this sense, it is worth noting that no dioxygen evolves when the sterically hindered 2,5-tert-butyl-p-benzoquinone is used rather than p-benzoquinone, showing a steric requirement in the hydrogen abstraction process.
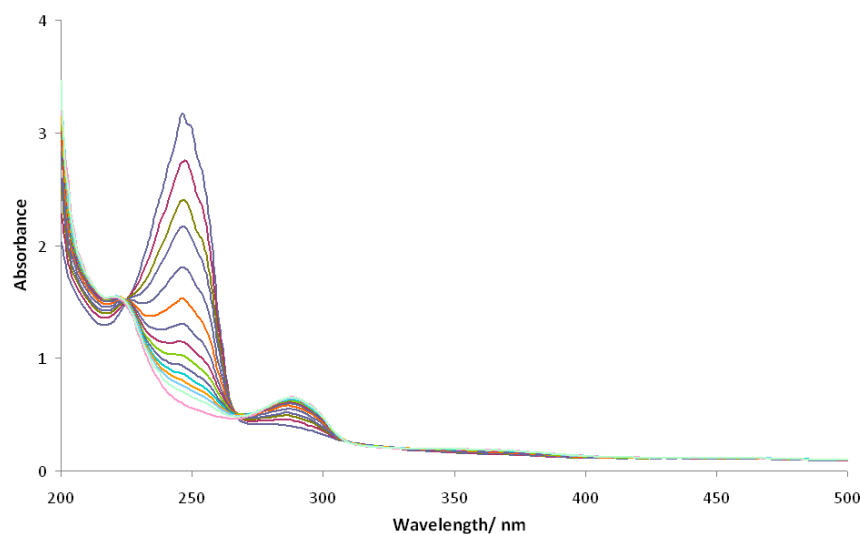
Figure 7. Ultraviolet spectra variation for p-benzoquinone during the water photolysis experiments using biocatalyst **1**, showing the decrease in the 246 nm band (disappearance of benzoquinone) and increase in the 290 nm band (formation of hydroquinone). Grey color corresponds to spectrum at time zero, and pink color corresponds to spectrum at 24 h.

3. Discussion

The results described in the previous section demonstrate that the selected ligands promote the formation of polynuclear structures: a Ba_2Mn_2 supramolecular box for **1** and a Mn_4N_6 planar-diamond cluster for **2** (Scheme S1). While the structural features of the biomimetic model **1** allow it to be a photolytic active compound, complex **2** is inactive. An explanation of these different catalytic behaviors can be found in the mechanism proposed by this catalysis. Previous studies with manganese(III)-Schiff base model systems using a comparable photolytic experimental setup showed that the photogeneration of dioxygen involves a mechanism with successive hydrogen abstractions from water molecules bound to the metal ion by optically excited p-benzoquinone. An H_2O molecule bound to the manganese ion starts off the reaction sequence by transferring a hydrogen atom to an O^- created by a $\pi^* \leftarrow n$ optical excitation in p-benzoquinone. This process oxidizes Mn(III) to Mn(IV) and creates tightly bound OH^- groups that are sufficiently polarized for easy deprotonation. The strong Mn–OH bond prevents the formation of hydroxylated rings, as occurs in aqueous solution in the absence of active Mn complexes. In the case of the present model complexes **1** and **2**, neither has a water molecule bound to the metal ions in the solid state. In the case of the biomimetic model **2**, there are two different environments around the metal ions: an octahedral geometry for Mn1, without any vacancy in the coordination sphere, and a trigonal bypiramidal for Mn2, which contains a chloride anion bound to the metal ion that could be, in principle, replaced by a water molecule. Most likely, the oxidation state of the metal ion (Mn(II)) does not favor the formation of hydroxide species required to trigger the reaction.

In complex **1**, a H_3L^1 ligand bridges two Mn(III) centers, providing a donor atom that occupies the apical position of the square-pyramidal coordination geometry. This apical coordination is rather weak, as demonstrated by the bond distances reported in Table 2. Thus, most likely, the weakly-coordinated bridging H_3L^1 ligand present in **1** dissociates, at least in part, in aqueous solution, generating an apical vacant position which allows the coordination of a water molecule. DFT calculations performed at the TPSSh/TZVP level (see computational details below) provide additional support for this hypothesis. Indeed, geometry optimizations of the $[MnL^1]^- \cdot 2H_2O$ entity provides a square pyramidal structure in which a water molecule occupies the apical position (Mn-O_{water} = 2.337 Å), with the ligand providing the four donor atoms of the basal plane with Mn-O and Mn-N distances of ca. 1.90 and 1.95 Å, respectively. These values are in good agreement with those observed in the X-ray structure (Table 2).

The second water molecule does not coordinate with the metal ion but remains involved in hydrogen bonding interactions with the phenolate oxygen atoms which highlights the preference of the metal center for a square-pyramidal coordination (Figure 8).
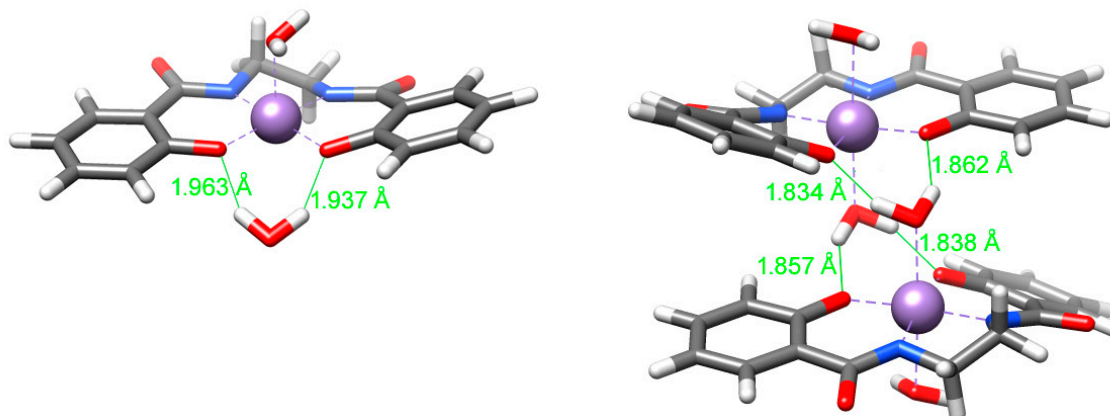

Figure 8. Geometries of the $[MnL^1]^-\cdot 2H_2O$ and $\{[MnL^1]^-\cdot 2H_2O\}_2$ systems obtained with DFT calculations (TPSSh/TZVP). The distances shown correspond to the hydrogen bonds involving water molecules.

We also employed DFT calculations to model the dimeric entity $\{[MnL^1]^-\cdot 2H_2O\}_2$, which is expected to be involved in the catalytic process (Scheme 1). According to our calculations (Tables S11 and S12), the formation of the $\{[MnL^1]^-\cdot 2H_2O\}_2$ entity is supported by hydrogen bonds involving coordinated water molecules and the phenolate oxygen atoms of a neighboring $[MnL^1]^-\cdot 2H_2O$ unit. The Gibbs free energy associated with the formation of the dimer from the monomer entity was calculated to be 6.0 kcal mol^{-1}, pointing to a sizeable stability of the $\{[MnL^1]^-\cdot 2H_2O\}_2$ edifice. The water molecules that bridge the two complex entities through hydrogen bonds are relatively close (3.42 Å), which likely facilitates the formation of oxygen upon deprotonation. Thus, the photolytic activity catalyzed by **1** likely follows a similar mechanism as that described above for manganese(III)-Schiff base model complexes, starting from μ-aqua dimers which suffer successive hydrogen abstractions in the presence of photoexcited p-benzoquinone. Photogenerated oxygen evolves in the overall process and μ-phenoxy dimers are proposed to form. The catalytic cycle involves the regeneration of the μ-aqua dimers through water coordination in both apical positions which is also consistent in aqueous media with previous published results [22] and present DFT calculation studies. A precipitate was not observed during or after the irradiation experiments catalyzed by **1**.

An alternative mechanism, without the need of μ-aqua dimers forms, was recently developed by Borovik et al. [50,51], who reported the feasibility of a sequential proton transfer-electron transfer route for converting a monomeric Mn^{IV}–OH to a Mn^{V}–oxo species, and also suggested that a single ligand can support mononuclear Mn complexes spanning four different oxidation states (II through V) with oxo and hydroxo ligands that are derived from water. These findings are also consistent with our previous proposed mechanism of multiple hydrogen abstractions from water molecules bound to the metal ion [22].

4. Materials and Methods

4.1. Chemical and Reagents

All of the starting materials (Aldrich) and solvents (Probus) used for the synthesis were of commercially available reagent grade and were used without further purification.

4.2. Physical Measurements

Elemental analyses were performed on a Carlo Erba Model 1108 CHNS-O (CE Instruments, Wigan, UK) elemental analyzer. The IR spectrum for **1** was recorded as KBr pellets on a Bio-Rad FTS 135 spectrophotometer (Bio-Rad Laboratories, Hercules, CA, USA) in the range 4000–400 cm^{-1}. IR spectrum for **2** was recorded as KBr pellets on a Varian FT-IR 670 spectrophotometer (Varian Medical Systems, Palo Alto, CA, USA) in the range 4000–200 cm^{-1}. ^{1}H NMR spectra were recorded on a Bruker AC-300 spectrometer (Bruker BioSpin, Rheinstetten, Germany) using CD$_3$OD (296 K) as solvent and SiMe$_4$ as an internal reference. The electro-spray mass spectra of the compounds were obtained on a Hewlett-Packard model LC-MSD 1100 instrument (Hewlett-Packard, Palo Alto, CA, USA) (positive ion mode, 98:2 CH$_3$OH–HCOOH as the mobile phase). Room temperature magnetic susceptibilities were measured using a digital measurement system MSB-MKI (Sherwood Scientific, Cambridge, UK), calibrated using mercury tetrakis(isothiocyanato)cobaltate(II) Hg[Co(NCS)$_4$] as a susceptibility standard. Electronic spectra were recorded on a Cary 230 spectrometer (Agilent Technologies, Stockport, UK). Conductivities of 10^{-3} M solutions in DMF were measured on a Crison microCM 2200 conductivimeter (Crison Instruments, Barcelona, Spain).

4.3. Synthesis of the Complexes

Ba$_2$Mn$_2$L^1$_2$(H$_3$L^1)$_2$(CH$_3$OH)$_4$ (**1**): 0.66 mmol (0.2 g) of H$_4$L^1 was dissolved in 50 mL of methanol and Ba(OH)$_2$ (0.66 mmol, 0.13 g), dissolved in 30 mL of methanol, was added to the initial light-colored solution. Then, a methanolic solution of Mn(Ac)$_2$.4H$_2$O (0.66 mmol, 0.16 g) was also added at room temperature. The initial light color of the solution rapidly changed to red-brown. After 3 h of stirring at room temperature, slow evaporation of the solvent led to the deposition of red crystals. The products were collected by filtration, washed with diethyl ether (2 × 20 mL) and then dried in vacuo. Yield: 0.12 g (43%). Selected data for **1**: MS(ESI): *m/z* 352.4 [MnL+ H$^+$]$^+$, 374.4 [MnL + Na$^+$]$^+$, 651.8 [MnL(H$_3$L) + H$^+$]$^+$, 706.6 [Mn$_2$L(H$_3$L) + H$^+$]$^+$, 789.0 [MnL(H$_3$L)Ba + H$^+$]$^+$, 926.2 [MnL(H$_3$L)Ba$_2$ + H$^+$]$^+$. Elemental analysis found: C, 47.5; H, 4.0; N, 6.5%. C$_{68}$H$_{70}$Ba$_2$Mn$_2$N$_8$O$_{20}$ (MW 1703.8) requires C, 47.9; H, 4.1; N, 6.6. IR (cm^{-1}) ν(O-H) 3407 (m), ν(amideI-H$_3$L$^-$) (C=O) 1641 (s), ν(amideI-L^{4-}) (C=O) 1605 (s), ν(amideII-H$_3$L$^-$) (C-N, N-H) 1551 (m), ν(amideII-L^{4-}) (C-N, N-H) 1540 (m), ν(C-O) 1243 (s). Magnetic moment μ_{eff} = 4.8 BM. ^{1}H NMR paramagnetic (DMSO-d$_6$, ppm): δ −24.165. $\lambda(\varepsilon)$ 510 nm (700).

Mn$_4$L^2$_6$Cl$_2$ (**2**): a methanol solution (40 mL) of MnCl$_2$ (40 mg, 0.2 mmol) was added dropwise to a CH$_3$OH/H$_2$O solution (20 mL) containing 2-cyanopyridine (42 mg, 0.4 mmol). The light green solution was heated for 40 min with stirring and then filtered after cooling to room temperature. Well-shaped colorless crystals of **2** suitable for X-ray diffraction were obtained within 2 months with a 25% yield upon slow evaporation of the solvents. Yield: 0.01 g (20%). Selected data for **2**: MS(ESI): *m/z* 1108.4 [**2** + H$^+$]$^+$, 1129.5 [**2** + Na$^+$]$^+$. Elemental analysis found: C, 45.1; H, 4.4; N, 14.9%. C$_{42}$H$_{48}$Cl$_2$Mn$_4$N$_{12}$O$_6$ (MW 1107.6) requires C,45.6; H, 4.3; N, 15.2%. IR (cm-1): IR (cm-1): ν (N-H carboxamide) 3237 (m), ν (C-H)$_{Ar}$ 3072 (m), ν (C-H)$_{Me}$ 2981 (w), 2940 (w), ν (C=NH carboxamide) 1659 (s), ν (C=N) 1631 (s), ν[(N=C–O–) + δ(NH)] 1379 (s), δ(O–CH3) 1206 (m), νas (C–O–C) 1138 (s), νs (C–O–C) 965 (m), ν (Mn-Cl) 303 (m).

4.4. X-ray Crystallographic Studies

Data for **1** and **2** were collected on a Bruker Smart CCD-1000 diffractometer (Bruker AXS GmbH, Karlsruhe, Germany) (at 100 K for **1** and at room temperature for **2**), using graphite-monochromated Mo–Kα radiation (λ = 0.71073 Å) from a fine-focus sealed tube source (at 100 K). The computing data and reduction were made by BRUKER SAINT (Bruker AXS GmbH, Karlsruhe, Germany) [52] software. In both cases, an empirical absorption correction was applied using SADABS [53].

The structures were solved by SIR-97 [54] and refined by full-matrix least-squares techniques against F^2 using SHELXL-97 [55]. Positional and anisotropic atomic displacement parameters were refined for all heteroatoms. The hydrogen atoms positions were included in the model by electronic

density, and they were refined isotropically [Uiso(H) = 1.2 Ueq(Atom)] or were geometrically calculated and refined using a riding model (isotropic thermal parameters 1.2–1.5 times those of their carrier atoms). The criteria for a satisfactory complete analysis were a ratio of "*rms*" shift to standard deviation of less than 0.001 and no significant features in the final difference maps. Molecular graphics were done with ORTEP [56] and Mercury [57]. A summary of the crystal data, experimental details, and refinement results are listed in Table 1. Significant bond distances and angles are summarized in Tables 2 and 3, while detailed crystallographic data is collected in Tables S1–S5 (for **1**) and Tables S6–S10 (for **2**).

4.5. Photolysis Experiments

The irradiation of aqueous solutions of complexes **1** and **2** was carried out in a colorless two-necked glass flask (1 L) placed in a methacrylate thermostatted water bath. Complex **1** (5×10^{-6} mol; 8.5 mg) was firstly dissolved in 2 mL of methanol, while 2 mL of dimethylformamide were used to prepare a solution of complex **2** (5×10^{-6} mol; 5.5 mg). A magnetically stirred solution of the biomimetic model and p-benzoquinone (2×10^{-4} mol; 21 mg) in 1 L of deoxygenated and deionized water was irradiated with light (in the 350–2500 nm range) from a 200 W tungsten lamp for 24 h. The solution was connected to a UV spectrophotometer through a peristaltic pump and a flow cell. Quantitative measurements of the amount of dioxygen formed during irradiation were performed using a dissolved oxygen probe-type electrode (Crison Oxi45P, Crison Instruments, Barcelona, Spain). In a typical experiment deionized deoxygenated water was placed in the two-necked glass flask—one neck contained the oxygen electrode and the second contained a septum. The whole flask arrangement was immersed in the thermostatted bath so that the water came up the base of the necks. Stirring was begun, the complex and quinone were added, and the septum was fitted to make the system airtight. Four needles were pushed through the septum—one reaching into the liquid—and a stream of dinitrogen was introduced into the solution until the reading of the oxygen meter fell to <3%. Once this value was reached, the N_2 needle and the purge needle were removed, and the system was left stirring for 10 min to equilibrate. The light was switched on. Only the two needles connected to the flow cell remained through the septum. Oxygen readings were recorded as % dissolved oxygen where 100% corresponds to a fully saturated aqueous solution at 25 °C (6 cm^3 O$_2$ dm^{-3}), and 0% corresponds to no dissolved oxygen. Reproducible results were obtained with this method provided that the temperature of the bath remained constant (25.0 $\pm$ 0.1 °C), and a constant stirring rate was maintained.

4.6. DFT Calculations

Full geometry optimizations of the [MnL^1]$^-$·2H$_2$O and {[MnL^1]$^-$·2H$_2$O}$_2$ systems were performed in aqueous solution employing DFT calculations at the TPSSh/TZVP [58,59] level employing the Gaussian 09 package (Revision D.01) [60]. Bulk solvent effects (water) were included by using the integral equation formalism variant of the polarizable continuum model (IEFPCM) [61]. No symmetry constraints were imposed during the optimizations. The stationary points found on the potential energy surfaces as a result of geometry optimizations were tested to represent energy minima rather than saddle points via frequency analysis. All calculations used an ultrafine integration grid and the default threshold for the SCF energy convergence (10^{-8} a. u.).

5. Conclusions

Two new biomimetic models of the OEC were prepared and characterized. DFT calculations show that the photocatalitically active Ba$_2$Mn$_2$ supramolecular box complex can follow a mechanism with successive hydrogen abstractions from water molecules bound to the metal ion by optically excited p-benzoquinone. In the case of the Mn$_4$N$_6$ planar-diamond cluster, the oxidation state of the metal ion (Mn(II)) does not favor the formation of hydroxide species required to trigger the photolytic reaction.

Bond lengths [Å] and angles [°] for **1**; Table S3: Anisotropic displacement parameters (Å^2 × 10^3) for **1**; Table S4: Hydrogen coordinates (×10^4) and isotropic displacement parameters (Å^2 × 10^3) for **1**; Table S5: Torsion angles [°] for **1**; Table S6: Atomic coordinates (×10^4) and equivalent isotropic displacement parameters (Å^2 × 10^3) for **2**; Table S7: Bond lengths [Å] and angles [°] for **2**; Table S8: Anisotropic displacement parameters (Å^2 × 10^3) for **2**; Table S9: Hydrogen coordinates (× 10^4) and isotropic displacement parameters (Å^2 × 10^3) for 2; Table S10: Torsion angles [°] for **2**. Table S11: Optimized Cartesian Coordinates (Å) obtained with DFT calculations (TPSSh/TZVP) for the [MnL^1]-2H2O system; Table S12: Optimized Cartesian Coordinates (Å) obtained with DFT calculations (TPSSh/TZVP) for the {[MnL^1]-2H2O}2 system; Scheme S1. Chemdraw structures for **1** and **2**; Figure S1: Paramagnetic ^{1}H NMR spectrum for complex 1; Figure S2: ESI mass spectrum for complex **2**; Figure S3: IR spectrum for **2**.

Author Contributions: Conceptualization, M.M.; Data curation, L.R. and D.E.; Formal analysis, M.I.F., R.P., L.M.B. and C.P.; Investigation, L.R., M.I.F. and R.P.; Supervision, M.M.; Writing original draft, L.R. and M.M.; Writing review & editing, L.M.B., D.E., C.P. and M.M.

Conflicts of Interest: The authors declare no conflict of interest.

Nomenclature

Acronyms

BQ	benzoquinone
DFT	density functional theory
DMF	dimethylformamide
DMSO	dimethyl sulfoxide
ESI-MS	electrospray ionization mass spectroscopy
NAPDH	nicotinamide adenine dinucleotide phosphate
NMR	nuclear magnetic resonance
ONNO	oxygen-nitrogen-nitrogen-oxygen
ORTEP	Oak Ridge thermal ellipsoid plot
SCF	self consistent field
TPSSh/TZVP	hybrid functional using the Tao-Perdew-Staroverov-Scuseria functional–valence triple zeta polarization basis set

References

1.   Umena, Y.; Kawakami, K.; Shen, J.R.; Kamiya, N. Crystal structure of oxygen-evolving photosystem II at a resolution of 1.9 Å. *Nature* **2011**, *473*, 55–60. [CrossRef] [PubMed]

2.   Yano, J.; Yachandra, V. Mn$_4$Ca cluster in photosynthesis: Where and how water is oxidized to dioxygen. *Chem. Rev.* **2014**, *114*, 4175–4205. [CrossRef] [PubMed]

3.   Chen, C.; Li, Y.; Zhao, G.; Yao, R.; Zhang, C. Natural and artificial Mn$_4$Ca cluster for the water splitting reaction. *ChemSusChem* **2017**, *10*, 4403–4408. [CrossRef] [PubMed]

4.   McEvoy, J.P.; Brudvig, G.W. Water-splitting chemistry of photosystem II. *Chem. Rev.* **2006**, *106*, 4455–4483. [CrossRef] [PubMed]

5.   Cox, N.; Pantazis, D.A.; Neese, F.; Lubitz, W. Biological water oxidation. *Acc. Chem. Res.* **2013**, *46*, 1588–1596. [CrossRef] [PubMed]

6.   Suga, M.; Akita, F.; Hirata, K.; Ueno, G.; Murakami, H.; Nakajima, Y.; Shimizu, T.; Yamashita, K.; Yamamoto, M.; Ago, H.; et al. Native structure of photosystem II at 1.95 Å resolution viewed by femtosecond X-ray pulses. *Nature* **2015**, *517*, 99–103. [CrossRef] [PubMed]

7.   Blakemore, J.D.; Crabtree, R.H.; Brudvig, G.W. Molecular catalysts for water oxidation. *Chem. Rev.* **2015**, *115*, 12974–13005. [CrossRef] [PubMed]

8.   Herrero, C.; Nguyen-Thi, N.; Hammerer, F.; Banse, F.; Gagné, D.; Doucet, N.; Mahy, J.P.; Ricoux, R. Photoassisted oxidation of sulfides catalyzed by artificial metalloenzymes using water as an oxygen source. *Catalysts* **2016**, *6*, 202. [CrossRef]

9.   Garrido-Barros, P.; Gimbert-Suriñach, C.; Matheu, R.; Sala, X.; Llobet, A. How to make an efficient and robust molecular catalyst for water oxidation. *Chem. Soc. Rev.* **2017**, *46*, 6088–6098. [CrossRef] [PubMed]

10. Paul, S.; Neese, F.; Pantazis, D.A. Structural models of the biological oxygen-evolving complex: Achievements, insights, and challenges for biomimicry. *Green Chem.* **2017**, *19*, 2309–2325. [CrossRef]

11. Dismukes, G.C.; Siderer, Y. Intermediates of a polynuclear manganese center involved in photosynthetic oxidation of water. *Proc. Natl. Acad. Sci. USA* **1981**, *78*, 274–278. [CrossRef] [PubMed]

12. Campbell, K.A.; Force, D.A.; Nixon, P.J.; Dole, F.; Diner, B.A.; Britt, R.D. Does aspartate 170 of the D1 polypeptide ligate the manganese cluster in photosystem II? An EPR and ESEEM study. *J. Am. Chem. Soc.* **2003**, *42*, 10600–10608. [CrossRef]

13. Satadal, P.; Cox, N.; Pantazis, D.A. What can we learn from a biomimetic model of nature's oxygen-evolving complex? *Inorg. Chem.* **2017**, *56*, 3875–3888. [CrossRef]

14. Rompel, A.; Andrews, J.C.; Cinco, R.M.; Wemple, M.W.; Christou, G.; Law, N.A.; Pecoraro, V.L.; Sauer, K.; Yachandra, V.K.; Klein, M.P. Chlorine K-edge X-ray absorption spectroscopy as a probe of chlorine-manganese bonding: Model systems with relevance to the oxygen evolving complex in photosystem II. *J. Am. Chem. Soc.* **1997**, *119*, 4465–4470. [CrossRef]

15. Grundmeier, A.; Dau, H. Structural models of the manganese complex of photosystem II and mechanistic implications. *Biochim. Biophys. Acta-Bioenerg.* **2012**, *1817*, 88–105. [CrossRef] [PubMed]

16. Askerka, M.; Brudvig, G.W.; Batista, V.S. The O_2-evolving complex of photosystem II: Recent insights from Quantum Mechanics/Molecular Mechanics (QM/MM), Extended X-ray Absorption Fine Structure (EXAFS), and Femtosecond X-ray Crystallography data. *Acc. Chem. Res.* **2017**, *50*, 41–48. [CrossRef] [PubMed]

17. Mullins, C.S.; Pecoraro, V.L. Reflections on small molecule manganese models that seek to mimic photosynthetic water oxidation chemistry. *Coord. Chem. Rev.* **2008**, *252*, 416–443. [CrossRef] [PubMed]

18. Yamaguchi, K.; Shoji, M.; Isobe, H.; Yamanaka, S.; Umena, Y.; Kawakami, K.; Kamiya, N. On the guiding principles for understanding of geometrical structures of the CaMn4O5 cluster in oxygen-evolving complex of photosystem II. Proposal of estimation formula of structural deformations via the Jahn-Teller effects. *Mol. Phys.* **2017**, *115*, 636–666. [CrossRef]

19. Maneiro, M.; Ruettinger, W.F.; Bourles, E.; McLendon, G.L.; Dismukes, G.C. Kinetics of proton-coupled electron-transfer reactions to the manganese-oxo "cubane" complexes containing the Mn_4O and Mn_4O core types. *Proc. Natl. Acad. Sci. USA* **2003**, *100*, 3707–3712. [CrossRef] [PubMed]

20. Liu, F.; Concepcion, J.J.; Jurss, J.W.; Cardolaccia, T.; Templeton, J.L.; Meyer, T.J. Mechanisms of water oxidation from the blue dimer to photosystem II. *Inorg. Chem.* **2008**, *47*, 1727–1752. [CrossRef] [PubMed]

21. Young, K.J.; Brennan, B.J.; Tagore, R.; Brudvig, G.W. Photosynthetic Water Oxidation: Insights from Manganese Model Chemistry. *Acc. Chem. Res.* **2015**, *48*, 567–574. [CrossRef] [PubMed]

22. González-Riopedre, G.; Fernández-García, M.I.; González-Noya, A.M.; Vázquez-Fernández, M.A.; Bermejo, M.R.; Maneiro, M. Manganese-Schiff base complexes as catalysts for water photolysis. *Phys. Chem. Chem. Phys.* **2011**, *13*, 18069–18077. [CrossRef] [PubMed]

23. González-Riopedre, G.; Bermejo, M.R.; Fernández-García, M.I.; González-Noya, A.M.; Pedrido, R.; Rodríguez-Doutón, M.J.; Maneiro, M. Alkali-metal-ion-directed self-assembly of redox-active manganese(III) supramolecular boxes. *Inorg. Chem.* **2015**, *54*, 2512–2521. [CrossRef] [PubMed]

24. Bermejo, M.R.; Fernández, M.I.; González-Noya, A.M.; Maneiro, M.; Pedrido, R.; Rodríguez, M.J.; García-Monteagudo, J.C.; Donnadieu, B. Novel peroxidase mimics: μ-Aqua manganese–Schiff base dimers. *J. Inorg. Biochem.* **2006**, *100*, 1470–1478. [CrossRef] [PubMed]

25. González-Riopedre, G.; Fernández-García, M.I.; Gómez-Fórneas, E.; Maneiro, M. Biomimetic catalysts for oxidation of veratryl alcohol, a lignin model compound. *Catalysts* **2013**, *3*, 232–246. [CrossRef]

26. Geary, W.J.; William, J. The use of conductivity measurements in organic solvents for the characterisation of coordination compounds. *Coord. Chem. Rev.* **1971**, *7*, 81–122. [CrossRef]

27. Daier, V.; Moreno, D.; Duhayon, C.; Tuchagues, J.; Signorella, S. Synthesis, characterization and combined superoxide dismutase and catalase activities of manganese complexes of 1,4-bis(salicylidenamino)butan-2-ol. *Eur. J. Inorg. Chem.* **2010**, 965–974. [CrossRef]

28. Collomb, M.N.; Mantel, C.; Romain, S.; Duboc, C.; Leprêtre, J.C.; Pécaut, J.; Deronzier, A. Redox-Induced μ-Acetato and μ-Oxo Core Interconversions in Dinuclear Manganese Tris (2-methylpyridyl) amine (tpa) Complexes: Isolation and Characterization of [Mn2III (μ-O)(μ-O_2CCH_3)(tpa) 2]$^{3+}$. *Eur. J. Inorg. Chem.* **2007**, 3179–3187. [CrossRef]

29.　Bonadies, J.A.; Maroney, M.L.; Pecoraro, V.L. Structurally diverse manganese (III) Schiff base complexes: Solution speciation via paramagnetic ^{1}H NMR spectroscopy and electrochemistry. *Inorg. Chem.* **1989**, *28*, 2044–2051. [CrossRef]

30.　Zuniga, M.F.; Deacon, G.B.; Ruhlandt-Senge, K. Developments in heterobimetallic s-block systems: Synthesis and structural survey of molecular M/Ae (M = Li, Na, K, Cs; AE = Ca, Sr) aryloxo complexes. *Inorg. Chem.* **2008**, *47*, 4669–4681. [CrossRef] [PubMed]

31.　Costes, J.P.; Laurent, J.P.; Chabert, P.; Commenges, G.; Dahan, F. Solid state and solution study of trinuclear (Ni, Ba, Ni) complexes: $(L^1{}_2Ni)_2Ba(ClO_4)_2\cdot2H_2O$ (**1**) and $(L^2{}_2Ni)_2Ba(ClO_4)_2\cdot2H_2O$ (**2**) (L^1 = 3-Methoxysalicylaldiminato and L^2 = 3-(2-Methoxyethoxy)salicylaldiminato). Crystal and Molecular Structure of 2. *Inorg. Chem.* **1997**, *36*, 656–660. [CrossRef]

32.　Jamnicky, M.; Segla, P.; Koman, M. Methanolysis of pyridine-2-carbonitrile in the coordination sphere of copper(II), cobalt(II) and nickel(II). The structure of [Ni(O-methylpyridine-2-carboximidate)$_3$]Br$_2\cdot$4H$_2$O. *Polyhedron* **1995**, *14*, 1837–1847. [CrossRef]

33.　Garduno, J.A.; García, J.J. Synthesis of annidines and benzoxazoles from activated nitriles with Ni(0) catalysts. *ACS Catal.* **2015**, *5*, 3470–3477. [CrossRef]

34.　Amami, V.; Ahmadi, R.; Naseh, M.; Ebadi, A. Synthesis, spectroscopic characterization, crystal structure and thermal analyses of two zinc(II) complexes with methanolysis of 2-pyridinecarbonitrile as a chelating ligand. *J. Iran. Chem. Soc.* **2017**, *14*, 635–642. [CrossRef]

35.　Devi, S.P.; Devi, R.B.; Devi, N.S.; Singh, L.J.; Singh, R.H. Structural and spectroscopic investigations on bis(1-amidino-*O*-2-alkoxyethylurea) copper (II) perchlorate complexes (alkoxy = methoxy, ethoxy or butoxy). *Polyhedron* **2012**, *47*, 1–8. [CrossRef]

36.　Amani, V.; Safari, N.; Khavasi, H.R. Synthesis, characterization and crystal structure determination of iron (III) hetero-ligand complexes containing 2,2′-bipyridine, 5,5′-dimethyl-2,2′-bipyridine and chloride,[Fe(bipy)Cl$_4$][bipy·H] and [Fe(dmbipy)$_2$Cl$_2$][FeCl$_4$]. *Polyhedron* **2007**, *26*, 4257–4262. [CrossRef]

37.　Paulat, F.; Praneeth, V.K.K.; Näther, C.; Lehnert, N. Quantum chemistry-based analysis of the vibrational spectra of five-coordinate metalloporphyrins [M(TPP)Cl]. *Inorg. Chem.* **2006**, *45*, 2835–2856. [CrossRef] [PubMed]

38.　Yang, C.I.; Lee, G.H.; Wur, C.S.; Lin, J.G.; Tsai, H.L. Syntheses, structures and single-molecule magnetic behaviors of two dicubane Mn$_4$ complexes. *Polyhedron* **2005**, *24*, 2215–2221. [CrossRef]

39.　Langley, S.K.; Chilton, N.F.; Massi, M.; Moubaraki, B.; Berry, K.J.; Murray, K.S. Synthesis and characterization of homo- and heterovalent tetra- hexa- hepta- and decanuclear manganese clusters using pyridyl functionalized *β*-diketone, carboxylate and triethanolamine ligands. *Dalton Trans.* **2010**, *39*, 7236–7249. [CrossRef] [PubMed]

40.　Wang, M.; Ma, C.B.; Yuan, D.Q.; Wang, H.S.; Chen, C.N.; Liu, Q.T. Synthesis and characterization of a family of penta- and tetra-manganese(III) complexes derived from an assembly system containing *tert*-butylphosphonic acid. *Inorg. Chem.* **2008**, *47*, 5580–5590. [CrossRef] [PubMed]

41.　Wemple, M.W.; Tsai, H.-L.; Wang, S.; Claude, J.P.; Streib, W.E.; Huffman, J.C.; Hendrickson, D.N.; Christou, G. Tetranuclear and octanuclear manganese carboxylate clusters: Preparation and reactivity of (NBu$^n{}_4$)[Mn$_4$O$_2$(O$_2$CPh)9(H$_2$O)] and synthesis of (NBu$^n{}_4$)2[Mn$_8$O$_4$(O$_2$CPh)$_{12}$(Et$_2$mal)$_2$(H$_2$O)$_2$] with a "linked-butterfly" structure. *Inorg. Chem.* **1996**, *35*, 6437–6449. [CrossRef] [PubMed]

42.　Ruettinger, W.; Yagi, M.; Wolf, K.; Bernasek, S.; Dismukes, G.C. O$_2$ Evolution from the manganese–oxo cubane core Mn$_4$O$_4{}^{6+}$: A molecular mimic of the photosynthetic water oxidation enzyme? *J. Am. Chem. Soc.* **2000**, *122*, 10353–10357. [CrossRef]

43.　Hendrickson, D.N.; Christou, G.; Schmitt, E.A.; Libby, E.; Bashkin, J.S.; Wang, S.; Tsai, H.L.; Vincent, J.B.; Boyd, P.D.W. Photosynthetic water oxidation center: Spin frustration in distorted cubane Mn^{IV}Mn$^{III}{}_3$ model complexes. *J. Am. Chem. Soc.* **1992**, *114*, 2455–2471. [CrossRef]

44.　Pedrido, R.; Bermejo, M.R.; García-Deibe, A.M.; González-Noya, A.M.; Maneiro, M.; Vázquez, M. Metal complexes of a novel achiral symmetric pentadentate ligand–Crystal structures of monohelical zinc(II) and cadmium(II) complexes. *Eur. J. Inorg. Chem.* **2003**, 3193–3200. [CrossRef]

45.　Addison, A.; Nageswara, R.T.; Reedijk, J.; Van Rijn, J.; Verschoor, G.C. Synthesis, structure, and spectroscopic properties of copper(II) compounds containing nitrogen–sulphur donor ligands; the crystal and molecular structure of aqua[1,7-bis(*N*-methylbenzimidazol-2′-yl)-2,6-dithiaheptane]copper(II) perchlorate. *J. Chem. Soc. Dalton Trans.* **1984**, 1349–1356. [CrossRef]

46. Awad, M.K.; Anderson, A.B. Photoactivation of H$_2$O by p-benzoquinone and the role of Mn^{III} complexes in O$_2$ evolution: Molecular orbital theory. *J. Am. Chem. Soc.* **1989**, *111*, 802–806. [CrossRef]

47. Ashmawy, F.M.; McAuliffe, C.A.; Parish, R.V.; Tames, J. Water photolysis. Part 1. The photolysis of coordinated water in [{MnL(H$_2$O)}$_2$][ClO$_4$]$_2$ (L = dianion of tetradentate O$_2$N$_2$-donor Schiff bases). A model for the manganese site in photosystem II of green plant photosynthesis. *J. Chem. Soc. Dalton Trans.* **1985**, 1391–1397. [CrossRef]

48. Aurangzeb, N.; Hulme, C.E.; McAuliffe, C.A.; Pritchard, R.G.; Watkinson, M.; Bermejo, M.R.; Garcia-Deibe, A.; Sanmartin, J.; Sousa, A. Crystallographic characterization of a possible model for photosystem II. *J. Chem. Soc. Chem. Commun.* **1994**, 1153–1155. [CrossRef]

49. Ononye, A.I.; McIntosh, A.R.; Bolton, J.R. Mechanism of the photochemistry of p-benzoquinone in aqueous solutions. 1. Spin trapping and flash photolysis electron paramagnetic resonance studies. *J. Phys. Chem.* **1986**, *90*, 6266–6270. [CrossRef]

50. Taguchi, T.; Stone, K.L.; Gupta, R.; Kaiser-Lassalle, B.; Yano, J.; Hendrich, M.P.; Borovik, A.S. Preparation and properties of an Mn^{IV}-hydroxide complex: Proton and electron transfer at a mononuclear manganese site and its relationship to the Oxygen Evolving Complex within Photosystem II. *Chem. Sci.* **2014**, *5*, 3064–3071. [CrossRef] [PubMed]

51. Gupta, R.; Taguchi, T.; Lassalle-Kaiser, B.; Bominaar, E.L.; Yano, J.; Hendrich, M.P.; Borovik, A.S. High-spin Mn-oxo complexes and their relevance to the oxygen-evolving complex within photosystem II. *Proc. Natl. Acad. Sci. USA* **2015**, *112*, 5319–5324. [CrossRef] [PubMed]

52. Bruker. *SAINT, Siemens Area Detector Integration Software*; Bruker AXS Inc.: Madison, WI, USA, 2003.

53. Sheldrick, G.M. *SADABS, Program for Scaling and Correction of Area Detector Data*; University of Göttingen: Göttingen, Germany, 1996.

54. Altomare, A.; Burla, M.C.; Camalli, M.; Cascarano, G.L.; Giacovazzo, C.; Guagliardi, A.; Moliterni, A.G.G.; Polidori, G.; Spagna, R. SIR97: A new tool for crystal structure determination and refinement. *J. Appl. Crystallogr.* **1999**, *32*, 115–119. [CrossRef]

55. Sheldrick, G.M. A short history of SHELX. *Acta Cryst.* **2008**, *A64*, 112–122. [CrossRef] [PubMed]

56. Farrugia, L.J. ORTEP-3 for Windows—A version of ORTEP-III with a Graphical User Interface (GUI). *J. Appl. Cryst.* **1997**, *30*, 565. [CrossRef]

57. Macrae, C.F.; Bruno, I.J.; Chisholm, J.A.; Edgington, P.R.; McCabe, P.; Pidcock, E.; Rodriguez-Monge, L.; Taylor, R.; van de Streek, J.; Wood, P.A. MERCURY CSD 2.0—New features for the visualization and investigation of crystal structures. *J. Appl. Crystallogr.* **2008**, *41*, 466–470. [CrossRef]

58. Tao, J.M.; Perdew, J.P.; Staroverov, V.N.; Scuseria, G.E. Climbing the density functional ladder: Nonempirical meta-generalized gradient approximation designed for molecules and solids. *Phys. Rev. Lett.* **2003**, *91*, 146401–146405. [CrossRef] [PubMed]

59. Schaefer, A.; Huber, C.; Ahlrichs, R. Fully optimized contracted Gaussian basis sets of triple zeta valence quality for atoms Li to Kr. *J. Chem. Phys.* **1994**, *100*, 5829–5835. [CrossRef]

60. Frisch, M.J.; Trucks, G.W.; Schlegel, H.B.; Scuseria, G.E.; Robb, M.A.; Cheeseman, J.R.; Scalmani, G.; Barone, V.; Mennucci, B.; Petersson, G.A.; et al. *Gaussian 09, Revision, A.01*; Gaussian, Inc.: Wallingford, CT, USA, 2009.

61. Tomasi, J.; Mennucci, B.; Cammi, R. Quantum mechanical continuum solvation models. *Chem. Rev.* **2005**, *105*, 2999–3094. [CrossRef] [PubMed]